Military Technical College
Kobry El-Kobbah,
Cairo, Egypt.

13th International Conference on Applied Mechanics and Mechanical Engineering.

EXPERIMENTAL AND COMPUTATIONAL INVESTIGATION OF THE AERODYNAMICS OF A SUPERSONIC PROJECTILE WITH STREAMWISE SLOTS

IBRAHIM* A. and FILIPPONE** A.

ABSTRACT

The present paper investigates the effect of streamwise slots applied to the boattail section of a projectile at supersonic speeds. Experimental work was performed to show the effect of the slots on the drag at Mach numbers M=1.36, 1.65 and 1.83. A single configuration of the slot pattern was used with two different slot widths (0.5mm and 2.0mm). The physics of the cavity flow was computationally investigated as well as the effect of the slots on the overall aerodynamic drag. Unlike the case of streamwise slots at transonic speeds, the suction and blowing mechanism is absent at supersonic speeds. It was found that there is a significant base drag reduction due to the presence of the streamwise slots. The reduction in total drag is modest when the width is W=0.5mm. However, the experiments showed that the drag increases at Mach numbers ranging from 1.36 to 1.83 for a slot width W=2.0mm.

KEY WORDS

Shock Wave, Boundary Layer, Base Drag, Streamwise Slots, Cavity Flow.

NOMENCLATURE

a	=peak-to-peak amplitude	t	=time
c_d	=total drag coefficient	U_∞	=free stream velocity
c_{db}	=base drag coefficient	u	=velocity in x-axis direction
c_{dsf}	=skin friction drag coefficient	v	=velocity in y-axis direction
c_p	=pressure coefficient	w	=velocity in z-axis direction
c_{pb}	=base pressure coefficient	W	=slot width
D	=projectile caliber, or drag force	y^+	=wall y^+ function
F_D	=predicted drag force	β	=boattail angle
F_i	=initial force	Δt	=time step
F_m	=measured force	Δx_{bt}	=distance between pressure taps at boat-

* Egyptian Armed Forces.
** Lecturer, School of Mechanical, Aerospace and Civil Engineering, University of Manchester, Manchester, U.K.

$f(t)$ =measured force with time
H =boundary layer shape parameter
k =turbulent kinetic energy
L =slot length
M =freestream Mach number
r =radius at the projectile base
tailed section
Δx_c =distance between pressure taps at cylindrical section
δ =boundary layer thickness
δ^* =boundary layer displacement thickness
θ =boundary layer momentum thickness
ψ =nozzle setting angle

INTRODUCTION

Range extension of artillery projectiles is an important issue to ammunition designers. There are different ways to extend the range of artillery projectiles; some of them depend on the weapon and others on the ammunition [1]. Drag reduction is one of the most reliable and economical ways to extend the range of artillery projectiles. This can be done by reducing the pressure drag on the projectile's fore-body or by reducing the base drag. For pressure drag reduction, increasing the ogive length and improving the nose shape are the typical methods followed to improve the ballistic shape of the fore-body. However, the base drag reduction is more effective, since it is the dominant component affecting the projectile at transonic and supersonic speeds [2]. Two different methods are used in order to get base drag reduction. The first is boattailing of the projectile blunt base, which is the simplest and effective way to get base drag reduction [3, 4]. The effectiveness of boattailing on the base drag stems from changing the initial conditions of the flow at the base corner before recirculation in the near wake region [5]. The second method consists in using a base bleed unit which is mounted to the projectile bottom. This unit contains a chemical composition that starts burning inside the weapon barrel and bleeds some gases up to 40% of the total time of flight. During this time, the base drag can be significantly decreased. However, the base bleed affects negatively the accuracy and dispersion of the point of fall, due to the difficulty in controlling the burning time of its chemical composition.

While boattailing is beneficial in decreasing the base drag, it has the disadvantage of increasing the pressure drag, due to the formation of normal shock wave at transonic speeds [6]. In order to decrease the damage effect of this shock wave on the boundary layer, the technique of passive flow control of shock wave/ boundary-layer interaction (SBLI) by applying porous walls was studied [6-9]. These studies showed that the porous walls applied to the boattail part produce a significant pressure drag reduction. However, using of a porous wall results in high viscous losses, as a result of increasing the boundary-layer thickness all over the area of SBLI. Moreover, the application of porous walls to the boattail part is not visible, due to the severe working conditions inside the weapon's barrel.

In 2002, a novel method of streamwise slots was suggested for the first time by Smith et al. [10]. The streamwise slots were applied to the upper surface of a DERA 2303 wing section. The results of wind tunnel tests revealed a smearing of the shock wave in the presence of streamwise slots which results in a wave drag reduction. This method was applied in place of the conventional method of SBLI by porosity, since the thickening of the boundary layer is confined to the slot width. Thus, limited viscous losses are incurred compared to those losses when using porous walls [11]. Recently,

the effect of the streamwise slots applied to a projectile was studied by the authors at transonic speeds [12]. Their study showed a significant base drag reduction by applying the slots configuration to the boattail part. Hereinafter, the effect of these slots is discussed at supersonic speeds to show to which extent they affect the total drag in this speed region.

EXPERIMENTAL SETUP

A. Test Facilities

The tests were performed in the supersonic wind tunnel at the Goldstein Laboratory at the University of Manchester. This wind tunnel is of an intermittent indraft type, which means that the flow in the test section is maintained by means of the pressure difference between the atmosphere and a vacuum tank. Two types of liners can be used: i) slotted-wall liners, which are used in transonic speed region up to Mach number of 0.86; ii) shaped liners, which were used for the first time in the present tests and were designed to get uniform supersonic speeds up to Mach number of 2.0. The area of the test section of this wind tunnel is 0.15x0.214 m^2. The area of the wind tunnel throat section can be changed through two plates attached to power screws rotated by two servo motors in order to control the flow speed in the test section. The run-time of the tunnel is 10 seconds at the maximum throat setting, which is corresponding to the wind tunnel's maximum speed.

B. Experimental Accuracy

Uncertainty analysis has been performed to show the accuracy of the predicted wind tunnel speed. The uncertainty of the Mach value is based upon the uncertainties of both the stagnation and upstream static pressures. Thus, the method of Kline & McClintock presented in Ref. [13] was applied in order to predict the Mach uncertainty. This was found to be 3.84% in the Mach number range $1.36 \leq M \leq 1.83$.

C. Wind Tunnel Models

Two half-scale bullet models were manufactured in order to get proper size suitable for the wind tunnel test section. The first model (M1) was used to measure the static pressure along the body. The second model (M2) was designed to measure the drag force using a force sensor integrated with the model assembly. The models were designed to be covered with skins having the required configuration (solid and slotted). These skins are assembled to the bullet body through 16 small screws.

1) Model M1

The first model was used in measuring the pressure distribution for both the solid and slotted-boattail bullets. As shown in Fig. 1, M1 consists of three main parts. The first is the ogive which is screwed to the second part (bullet body). The third part is the connecting tube used to connect M1 with the sting inside the wind tunnel test section. The model was designed to pass the pressure tubes through the grooves that were cut into the bullet body and the connecting tube. The skin covering the boattail section can be changed to be solid one or those with the streamwise slot patterns.

The static pressure measurements were performed through twelve pressure taps on both the cylindrical and boattail sections of the model. These pressure taps were connected to 26PCDFA6D Honeywell pressure sensors. The pressure taps were made at seven stations on the cylindrical section and five stations on the boattail section as shown in Fig.2. It can be noted that the positions of the pressure taps on the boattail part are not extended to be aligned with the end of the slots, since the groove underneath the skin cannot be extended more than this limit. The groove length is limited because of the shoulder which is required to machine the screws' threads for fixing the skins to the boattail part. Moreover, there is a place at the end of the boattail for a grub screw to fix the model with the connecting tube.

2) Model M2

Figure 3 illustrates assembled and exploded views of M2. Two linear bushes (5) are mounted inside the bullet body (3). The ground shaft (4) passes through these linear bushes to move freely in the axial direction. The circlip (6) is used to limit the movement of the shaft in freestream direction. The force sensor (7) is fixed to the holder (8) through two grub screws (11). The shank of the holder passes through a linear bush (9) which is mounted inside the rear part of ogive (2). This part of the ogive is screwed to the bullet body (3). The regulating bolt screwed to the rear part of the ogive passes through a hole in the shank of the sensor holder (8) to lean on one face of the sensor (7). The other face of the sensor is in contact with the face of the ground shaft. Initial force can be given to the force sensor by screwing the regulating bolt. Two holes were drilled in the bullet body (3) to allow passing of the electrical wires that are connected to the sensor's legs. Figure 4 displays photos of the M1 inside the wind tunnel test section and both of M1 and M2 with half of the skins taken off. An insulator around the cavities' bottoms in M2 was used to prevent any short circuits between the electrical wires connections. The exit wires are of varnished type to decrease the side effect on the base flow.

3) Skinning of the Models

The skins of the cylindrical and boattail sections were rolled manually by using a rolling device. The skins were cut first from a metallic sheet (deep drawing steel), then the required slot pattern was machined easily at the skins before rolling. The effect of rolling on the slot width was neglected. Figure 5 displays the rolling device and the skins before and after rolling. The rolling tool was designed for rolling the cylindrical and boattail skins.

This device consists of seven main parts. The shaft (1) which is fixed to a vice at one of its ends and the remaining parts can be rotated easily around that shaft. Roller (7) has the shape of a truncated cone having half apex angle equal to the boattail angle. It rolls around the machined part of the shaft (1) which is similar to the boattail part. Half of the boattail skin is cut from a metallic sheet then it is fixed to the shaft (1) through two screws. By rotating the roller (7) using the handle (4), the skin (8) can be shaped to fit its place on the boattail. To keep the skin specimen squeezed to the shaft (1) during rotation, the handle (4) was threaded from the end connected to the roller holder (5). This threaded part is screwed into block (3). Thus, before rolling, the handle should be screwed to keep firm contact between the roller (7) and the shaft (1). The roller holder (5) is guided by the pin (6), which passes through the bracket (2). The shaft (1) and the

sub-assembly of the roller (roller, roller holder and guiding pin) were replaced by their counterparts in case of rolling the cylindrical skin.

COMPUTATIONAL DETAILS

The computational investigation in this study was carried out by applying the Reynolds-averaged Navier-Stokes equations (RANS) in time-independent form using the commercial code FLUENT. The coupled-implicit scheme was used to solve the system of differential equations. The second-order upwind scheme was used in discretizing the spatial dependent properties in RANS equations. Shear stress transport k-ω turbulence model [14] was used in this study.

The present study deals with a secant-ogive-cylinder-boat-tail (SOCBT) bullet, which is similar to the typical shape of the artillery projectiles. The relative dimensions in terms of the bullet caliber D are shown in Fig. 6. The skin of the boat-tail part is cut by 8 slots which are homogeneously distributed around the circumference. A 4.0mm cavity depth is underneath the 0.80mm thick slots' skin. The length of the slot (L) is equal to half of the caliber D. Two slot widths were tested in this study, W=0.5 and 2.0mm.

A. Grid Generation

Performing a robust and accurate CFD calculation requires the optimization between the grid size and its quality. On the one hand, the grid size should be minimized in order to get robust simulation. On the other hand, the grid quality should be taken into consideration to get accurate and converged solution. A grid independent studies is the only way to achieve these two basic aspects. The key result that was monitored in the grid sensitivity study is the total drag coefficient. [12].

1) Solid-Wall Projectile

To match its counterpart in case of slotted-wall bullet, the domain around the solid-wall one was divided into eight sectors. Then, one sector was selected to be the computational domain. Figure 7 shows an overall view of the structured grid of hexahedral/wedge cells as well as a detail view for the mesh over the cylindrical part. The structured grid is more economical in the present case since a much larger aspect ratio (up to 140 near the solid walls and less 50 around the slot opening) than tetrahedral cells can be used. To resolve the viscous sub-layer, the height of the cells adjacent to the projectile surface was taken equal to 7.2×10^{-5} D. The cells were stretched towards the pressure far field by a ratio equal to 1.15. The value of wall function $y^+ < 1.0$ for the wall adjacent cells was checked to confirm the sufficient resolution of the mesh near the wall.

Five grids were tested on the solid projectile at a Mach number of 0.96 to obtain the grid independent solution [12]. The coarsest grid consists of 270,600 cells. Figure 8 shows the variation of the total drag coefficient with the grid size normalized by the number of cells for the used grid (NG). The fourth grid is that one for the solution independency since there is insignificant change in the drag coefficient from grid four to grid five. Thus, a mesh of 627,000 cells was used with streamwise spacing $\Delta x < 0.3\delta$ at the region of SBLI, where δ is the boundary-layer thickness upstream of the position of interaction on the cylindrical part.

2) Slotted-Wall Projectile

Many steps were required to generate the mesh of the slotted-wall projectile starting by that one around the solid-wall projectile. Then the grid was generated in the cavity-slot arrangement using hexahedron cells. Finally, the grids were merged together.

It is known a priori that a finer mesh is required in the region around the slot. This region was refined until the solution showed a negligible change in total drag coefficient, using grid adaptation technique which has been performed in Ref. [12]. Two stages of region adaption of the grid were performed. Two coaxial cylindrical regions were constructed around the slot. Therefore, the number of faces on the slot opening is duplicated each time of region adaptation to get 8 cells per 0.5mm slot width and 16 cells per 2.0mm width slot. After refinement of the grid around the slot, the final mesh size in case of W=0.5 and 2.0mm is 1.2 and 1.6 million cells, respectively. Figure 9 displays the refinement of the mesh around the slot on a longitudinal plane passing through the middle of the slot opening.

B. Boundary Conditions

Figure 10 displays the boundary conditions which are: the pressure far field boundary on the uniform upstream flow at a distance equal to 23 D, the symmetric boundary on both sides of the computational domain, and the adiabatic no-slip conditions on the solid projectile wall as well as the walls of the cavity-slot arrangement.

To construct a structured mesh, it is required to divide the computational domain into two main blocks. The first block is over the solid-wall surfaces and the second one is around the slotted-boattail surface. The two blocks were merged through the interface boundary condition to get the mesh in its final form.

RESULTS AND DISCUSSIONS

A. Pressure Measurements

The flow speed inside the wind tunnel can be controlled by changing the area of the second nozzle (diffuser area) through two swiveled plates connected to two servo motors as shown in Fig. 11. The area of the nozzle is inversely proportional to the nozzle setting angle (ψ). Before performing the experimental work, the relationship between ψ and M in the wind tunnel test section was determined. Figure 12 displays this relationship in the two cases: i) when there is no model in the wind tunnel test section (dotted line), and ii) when the present model is fixed to the sting in the test section (solid line). These lines were determined by linear fitting of the measured Mach numbers at different angles of the nozzle. The marked points on the same figure are the measured Mach numbers corresponding to the nozzle setting in case of fixing the present model inside the test section.

The surface static pressure distribution was measured at a Mach number M=1.36 for the solid-wall bullet and for the bullet provided with slotted boattail. Part (a) of Fig. 13 shows the measured and calculated pressure coefficients along the cylindrical and boattail sections of a solid projectile. Locations of pressure taps are shown in Fig. 2. There is a good agreement between the measured and calculated pressures except, at the second pressure taps on the cylindrical and boattail parts. It is thought that the

pressure rise is due to shock waves generated due to the existence of the line separating the bullet body and the skins of the cylindrical and boattail sections.

Parts (b) and (c) of the same figure display a comparison between the measured and calculated pressure coefficients on a slotted boattail with slot thicknesses 0.5 and 2.0mm, respectively, at M=1.36. There is a pressure rise at the second point of measurement in each case. It is thought that the pressure jump is due to the same reason as in the solid wall.

B. Effect of Streamwise Slots on the Flow past the Boattail

Hereinafter the effect of the streamwise slots on the flow past the boattail at M=1.36 will be discussed through a comparison with its counterpart in case of solid boattail. Mach contours around the bullet for both solid and slotted boattails are illustrated on the left of Fig. 14. The contours are displayed on a longitudinal plane passing through the middle of the slot in case of slotted bullet, whatever the slot width. The right graphics displays details of these contours around the boattail section only. It is obvious that there is no effect of the slots upstream the boattail part. Weak shock waves can be seen at the end of the slots in case of W=0.5 and 2.0mm. However, the contours are smeared on the slotted boattail compared with the solid one. Smearing of Mach contours is usually accompanied by the formation of a pressure plateau. This can be detected from the distribution of pressure coefficients along the slot centre line, as it is explained in Fig. 15.

Figure 15 displays a comparison between the distribution of pressure coefficients for both solid and slotted boattails. For the slotted boattails, the pressure coefficient distribution is shown at two different locations. The first is along a line passing through the middle of the slot opening and the second is along a line passing through the mid-distance between two successive slots. By looking at the pressure distributions on the slotted wall in both of the cases, it is observed that the pressure distribution is going to that distribution over the solid wall. This can be detected from decreasing of the extension of pressure plateau as going away from the middle of the slot. However, there is a sudden pressure rise before the end of the slot. This pressure rise results from a weak shock wave at the slot end. The shock wave is formed with the sudden change in the streamlines directions towards the cavity just before the end of the slot.

Figure 16 displays the u-v streamlines past the boattail and inside the cavity along a vertical plane passing through the slot centre line. There is a separating plane at the interaction between the main flow and the cavity flow. This plane starts approximately from the station number 1 up to station number 6 in both of the slotted-wall configurations. The direction of the flow inside the cavity at these stations shows a tendency towards exiting the slot opening. However the main flow is strong enough to change the direction of the secondary flow to be in the streamwise direction. This interaction between the two flows creates a slip plane which has variable locations in the slot neck or immediately above the slot opening. At station 7, the flow starts to recirculate inside the cavity, and ends by a vortex attached to the cavity floor. The recirculation of the streamlines shows stronger flow inside the cavity in case of W= 0.5mm than that flow in case of W=2.0mm. This can be noted from the upstream movement of the vortex in case of W=0.5mm.

Figure 17 illustrates the flow patterns inside and above the cavity through v-w streamlines at seven stations. The positions of these stations are shown in Figs. 16. Before going through the details of the flow across these sections, two major aspects are noted in the sections 1 to 6. The first aspect is the tendency of the flow direction to leave the cavity. The second is the formation of the slip plane that appears as a separating arc in the slot neck, or immediately above the slot opening. However, for the last section (S.7) in both the two cases it can be seen that suction of the flow inside the cavity is very similar to the slit suction in case of boundary layer removal.

Figures 18 to 20 show sketches of the flow pattern across the aforementioned stations. In particular, Fig. 18 illustrates the general behavior of the flow at sections 1 to 5 in case of W=0.5mm and stations 1 to 6 in case of W=2.0mm. This sketch was drawn in terms of the flow pattern in S.5 in each case, since it has all of the explained features. In general, the flow pattern across these stations is characterized by opposite-circulation vortex pair (VP.1) of conical type, which is extended along the cavity till the recirculation of the flow inside the cavity. The locations of the vortex cores change according to its strength. Two saddle points (SD.1 and SD.2) can be seen between the cores of VP.1. The saddle point SP.1 does not exist at some stations, due to changing of the vortex strength. At S.3 in case of W=0.5mm, a third point can be seen and the vortex disappears at S.4 in case of W=2.0mm. It is thought that the features of the flow are different at these sections because of the interaction with the vortex shown in Figs. 16. The slip plane represents a barrier preventing the out flow of the slot opening. Thus, this plane is almost changing its location at the slot neck.

Figure 19 illustrates the flow pattern at S.6 in case of W=0.5mm. The formation of the primary vortex VP.1 can be observed with the saddle point SP.1 between its cores. However, the start of formation of a secondary vortex VP.2 can be noticed. This vortex is not complete in that frame since its streamlines are not closed loops as shown in part (b) of the same figure.

Figure 20 displays the flow streamlines inside the cavity at S.7 in case of W=0.5mm. At this station the flow enters the cavity and the formation of the primary vortex VP.1 can be seen with its saddle point SP.1. Meanwhile, the secondary vortices are formed (VP.2 and VP.3). The formation of the secondary vortex near the slot corners is shown in Fig. 21-a. This vortex is formed as a result of the flow separation near the slot edges. Part (b) of Fig. 21 illustrates the formation of the vortex VP.3. It is speculated that the formation of this vortex is due to the high entrance speed of the flow through the slot, which results in regions of flow separation at the cavity floor in the spaces between two successive slots. In case of W=2.0mm, the flow entrance speed is relatively small compared with that one in case of W=0.5mm. Thus, there are no regions of flow separation near the slot edges or near the cavity floor; consequently, the formation of secondary vortices is absent in this case at S.7.

Figure 22 shows the boundary-layer velocity profiles for the solid and slotted-wall boattails at successive stations starting from the cylinder-boattail junction. These stations are located at a longitudinal plane passing through the middle of the slot. The upper part of this figure displays a comparison between the velocity profiles for the solid and slotted-wall bullets with W=0.5mm, and the lower part for W=2.0mm. At station 1 and 2, the difference between the velocity profiles is negligible. Nevertheless, at stations 3 to 6, there are some differences in the velocity gradients, since these stations are located at the slot opening. The velocity gradient ($\partial u/\partial y$) in case of both the slotted

boattails is less than that at solid wall. Moreover, it can be seen that $\partial u/\partial y$ for the velocity profiles in the case of the slotted boattail with W=2.0mm is less than those profiles for the slotted wall with W=0.5mm. The decrease in velocity gradients in case of slotted boattails is due to the lower viscous shear stresses above the slot opening, since the main flow moves on the secondary flow in the slot neck, which is smoother than the solid surfaces resulting in drop in viscous shear stresses. Figure 23 gives an indication about the viscous shear stresses calculated along the solid boattail, as well as the slotted ones. In the case of the slotted boattails, the shear stress is calculated along a line passing through the middle of the slot. It is shown that there is a sudden drop in the shear stress above the slot opening. This is in agreement with the boundary-layer velocity profiles past both the solid and slotted bullets.

The distinctions in the boundary-layer velocity profile gradients result in differences in the boundary-layer thicknesses. At transonic speeds, it is known that the main reason for boundary-layer thickening in any recirculating cavity flow device is the blowing of the secondary flow from the upstream side of the slot opening. Suction/blowing mechanism is absent in the case of slotted boattail at M=1.36, since the adverse pressure gradient past the boattail is not enough to activate this mechanism. However, there is slit suction through a recirculating flow at the slot end which results in a thinner boundary-layer just before the end of the slot. Therefore, a development of a new boundary-layer starts again after the main flow passes the slot end consequently, the boundary-layer will be thinner at the base corner compared with the solid boattail.

C. Effect of Streamwise Slots on the Flow behind the Base

Figure 24 shows the mean axial velocity distribution behind the base for the solid and slotted bullets. The position of the rear stagnation points can be seen where the axial velocities vanish. A movement of the rear stagnation points downstream can be noted when the solid boattail is provided with slot pattern, whatever the width of its slots. That means there is an expansion of the near wake region behind the slotted boattails. This expansion can be detected from the u-v streamlines shown in Fig. 25. The expansion of the near wake region behind the base is accompanied by lower growing rate of the free shearing layers, resulting in reduced entrainment in the recirculation region. These features of the near wake region are consistent with higher base pressure [5].

Figure 26 displays the contours of the axial velocity component (u/U_∞) behind the base for both the solid and slotted boattails. In the case of W=0.5mm, for the slotted boattail, the contours are shown at a longitudinal plane passing through the middle of the slot. Lower velocity gradients can be observed in the case of the slotted boattail. This behavior can be noted near the base, for instance, where the two successive contours of values -0.1886 and -0.0434 are generally closer in case of the solid wall. Thus, the free shear layers in the case of the slotted boattail have lower growth rate, which means an increase in wake contraction angle (the angle between the base and the maximum friction line).

Figure 27 illustrates the turbulent kinetic energy (k/U^2_∞) contours for both the aforementioned two cases. A higher turbulence level can be observed in the near wake region in case of solid boattail, since the maximum turbulent kinetic energy is 0.0468 against 0.0413 in case of the slotted boattail. It means that approximately 12% drop in the peak of turbulence level can be obtained by applying the slots to the boattail. Adding to that, there is a shift of that peak towards the rear stagnation (RS) point in

case of the slotted boattail. Turbulence level reduction and movement of its peak downstream means less mass entrainment from the recirculation region in the near wake zone, which is accompanied with higher base pressure in case of slotted boattail. Increasing the base pressure leads to base drag reduction. The same behavior of the base flow in case of a bullet provided with a slotted pattern of 2.0mm width was found to be similar to that behavior in case of W=0.5mm.

Table 1 shows the properties of the boundary-layer profile at station 8, which is shown in Fig. 22. These properties are the initial conditions for the free shearing layers developing after the base corner. By comparing the boundary-layer thicknesses, it can be found that the boundary-layer of slotted boattails is thinner than its counterpart in case of a solid one. This decrease in boundary-layer thickness is due to the development of a new boundary-layer at the slot end after recirculation in the cavity which is similar to boundary-layer slit suction. It is very interesting to notice that there is an increase of the boundary-layer shape factor (H) in case of slotted wall. While the shape factor is a function of the history of the incoming boundary-layer [15], this increase in (H) tells that some disturbance happens before the flow reaches the base corner. The disturbance is the recirculating flow at the slot end which is very similar to the boundary-layer bleed through slit suction.

Figure 28 shows the pressure coefficient behind the bullet base for both the solid and slotted boattails. It can be seen that there is higher base pressure in case of the slotted boattails, whatever the slot width. This increase in base pressure results in base drag reduction by 9.0% and 11.0% in case W=0.5 and 2.0mm, respectively.

D. Force Measurements

The Honeywell force sensor FSG-15N1A was used for measuring the drag force. Before its assembling with M2, the sensor was calibrated to find the linear relation between the measured voltage and the applied load. Figure 29 displays the typical behavior of the recorded signal during measuring the force. Oscillations with small amplitudes can be observed from the zero time up to the instant of firing the tunnel at time t_1. The sudden flow of the air causes vibration of the model inside the test section, resulting in amplified oscillations from the instant t_1 up to damping these oscillations at time t_2. Then, from the instant of time t_2 to the instant of shut down the flow at time t_3, the measured force oscillates around an average value. Then, the model vibrates again due to the sudden shut down of the air flow causing quick damped oscillations.

The number of the measured sample is 400 per second, which means a time step Δt of 2.5×10^{-3}. This gives an acceptable statistical uncertainty analysis while the time period (t_3-t_2) of measuring the force is more than one second for all of the cases. Thus, averaging the measured force could be reliable with Mach numbers higher than 1.36. Many trials had been done to measure the drag force below this Mach number, but the oscillations increased and led to unreliable data ensembles. The peak-to-peak amplitude (a) was found to be in the order of the estimated force itself at Mach 1.3. It is thought that the small area of the test section is the main reason of these oscillations, because of the shock waves reflections which generate at this critical Mach speed in the transonic region.

Figure 30 displays the measured values of the drag on bullets with solid and slotted boattails at Mach numbers equal to 1.36, 1.65 and 1.83. The moment of firing the

tunnel is marked by number 1 (corresponding to time t_1) while the moment of shut down the flow inside the tunnel is marked by number 0 (corresponding to time t_3). It can be seen that the peak-to-peak amplitude of the oscillations within the time period t_3-t_2 decreases with the Mach number. In some cases, it is also noticed that the initial force F_i before firing the tunnel is not the same value as that value after shutting down the flow. It is thought that the drop in the flow temperature and the highly damped oscillations at the moment of shut down affect the tolerances of the model assembly, resulting in changing of the initial force. This change in the initial force is negligible and doesn't affect the measured values, since the drag force is estimated from the difference between the measured force F_m in the time period t_3-t_2 and the initial force F_i in the time period t_1.

The drag can be estimated by averaging of the recorded signals. Averaging the measured force in the time period t_1 was performed to calculate the initial force F_i,

$$F_i = \frac{1}{t_1}\int_0^{t_1} f(t)\,dt. \qquad (1)$$

Averaging the measured force in the time period $t_3 - t_2$ was done for predicting F_m,

$$F_m = \frac{1}{t_3 - t_2}\int_{t_2}^{t_3} f(t)\,dt. \qquad (2)$$

The drag is calculated by subtracting the initial force (F_i) from the measured force (F_m);

$$F_D = F_m - F_i \,. \qquad (3)$$

Based on the experimental results, Fig. 31 illustrates a comparison between the measured drag on M2 with solid boattail and with slotted boattails at W=0.5 and 2.0mm. By comparing the measured forces in both of the slotted boattail cases with the solid one, a modest drag reduction up to 2.36% in case of W=0.5mm is found, and a slight increase in the drag up to -4.07% in case of W=2.0mm. By comparing the measured and calculated drag [listed in Table 2] it can be found that the CFD results overestimate the wind tunnel data. This difference is due to the existence of the sting and the frictional forces during measurements. Moreover, the computational results show insignificant drag reduction by using streamwise slots applied to the boattail at Mach number of 1.36.

According to the uncertainty analysis of force measurements, it was found that the maximum uncertainty value occurs at M=1.36 and is equal to 2.4%. This uncertainty is in the same order of the drag reduction (2.36%) and is approximately half the absolute value of the predicted increase in drag (-4.07%). Thus, the computational results could be rather decisive in assessment of the effectiveness of streamwise slots on the drag at supersonic speeds. The effect of streamwise slots on the drag of both solid and slotted

bullets at M=1.36 is quantitatively shown through the data listed in Table 2. Although there is a base drag reduction in both of the bullets with slotted boattail compared with the solid one, this reduction is offset by the increase of the boattail drag. Thus, the total effect of the streamwise slots on the total drag of the bullet at supersonic speeds is insignificant.

CONCLUSIONS

Experimental and computational studies were performed to investigate the effect of streamwise slots applied to the boattail part of an OSCBT bullet at supersonic speeds. The results showed that the suction/blowing mechanism is absent at this speed region, since the adverse pressure gradient is not strong enough to initiate this mechanism through the slot opening. The study of the boundary-layer velocity profiles and flow pattern at M=1.36 was thoroughly investigated. It was found that the flow causes recirculation inside the cavity after entering through the slot opening at its end. Thus, a part of the low momentum flow of the boundary layer is sucked through the slot opening and a lower velocity gradient are obtained; consequently, lower boundary layer thickness as well as its characteristic thicknesses. The drag was not affected significantly by applying the streamwise slots at this speed region. Although there is a base drag reduction, the increase in the boattail pressure drag offsets this reduction. It means that the final effect of the streamwise slots on the total drag is insignificant at supersonic speeds.

REFERENCES

[1] Karsten, P. A., "Long Range Artillery: The Next Generation," 17th International Symposium on Ballistics, Midland, South Africa, pp. 133-141, (1998).
[2] Tanner, M., "Reduction of Base Drag," Progress in Aerospace Sciences, Vol. 16, No. 4, pp. 369-384, (1975).
[3] Fu, J. and Liang, S., "Drag Reduction for Turbulent Flow over a Projectile: Part I," Journal of Spacecraft and Rockets, Vol. 31, No. 1, pp. 85-92, (1994).
[4] Platou, A. S., "Improved Projectile Boattial," Journal of Spacecraft, Vol. 12, No. 12, pp. 727-732, (1975).
[5] Herrin, J. L. and Dutton, J. C., "Supersonic Near-Wake Afterbody Boattailing Effects on Axisymmetric Bodies," Journal of Spacecraft and Rockets, Vol. 6, pp. 1021-1028, (1994).
[6] Liang, S. and Fu, J., "Drag Reduction for Turbulent Flow over a Projectile: Part II," Journal of Spacecraft and Rockets, Vol. 31, No. 1, pp. 93-98, (1994).
[7] Hsiung, J. and Chow, C., "Drag Reduction of Transonic Projectile by Porous Surface", AIAA Paper 93-0417, (1993).
[8] Hsiung, J. and Chow, C., "Computed Drag Reduction on a Projectile Using Porous Surfaces," Journal of Spacecraft and Rockets, Vol. 32, No. 3, pp. 450-455, (1995).
[9] Liang, S. and Fu, J., "Passive Control Method for Drag Reduction for Transonic Projectiles", AIAA Paper 91-3213-CP, (1991).
[10] Smith, A. N., Babinsky, H., Fulker, J. L., and Ashill, P. R., "Experimental Investigation of Transonic Aerofoil Shock/Boundary Layer Interaction Control Using Streamwise Slots," Proceedings of the IUTAM Symposium Held in

Gottingen, Germany, Kluwer Academic Publishers, Dordrecht, The Netherlands, pp. 285-290, (2002).
[11] Smith, A. N., Babinsky, H., Fulker, J. L., and Ashill, P. R., "Shock-Wave/Boundary-Layer Interaction Control Using Streamwise Slots in Transonic Flows," Journal of Aircraft, Vol. 41, No. 3, pp. 540-546, (2004).
[12] Ibrahim, A. and Filippone, A., "Effect of streamwise slots on the Drag of a Transonic Projectile," Journal of Aircraft, Accepted for Publication, (2007).
[13] Kline, S. J. and McClintock, F. A., "Describing Uncertainties in Single Sample Experiments," Mechanical Engineering, Vol. 75, No. 1, pp. 3-8, (1953).
[14] Menter, F. R., "Two-Equation Eddy-Viscosity Turbulence Model for Engineering Applications," AIAA Journal, Vol. 32, No. 8, pp. 1598-1605, (1994).
[15] Delery, J. M., "Shock Wave/Turbulent Boundary Layer Interaction and its Control," Progress in Aerospace Sciences, Vol. 22, No. 4, pp. 209-280, (1985).

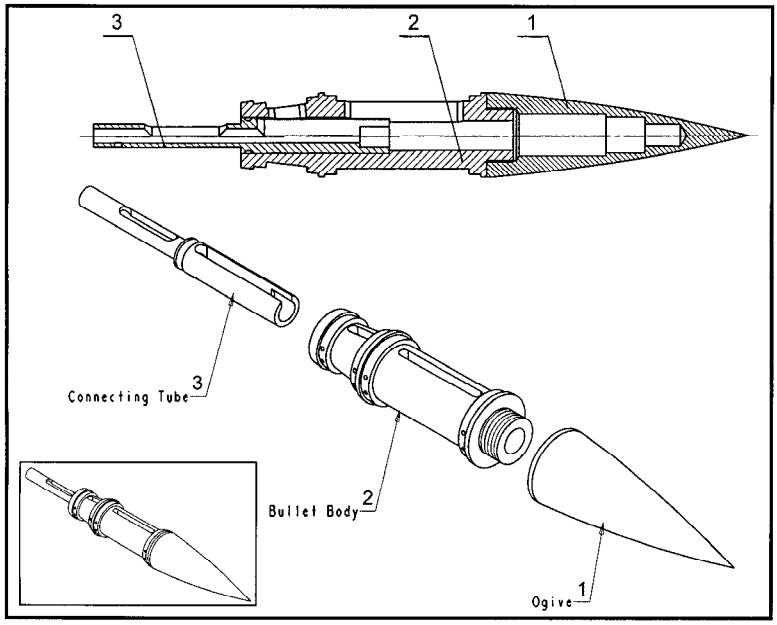

Fig.1 Assembly drawing of model M1

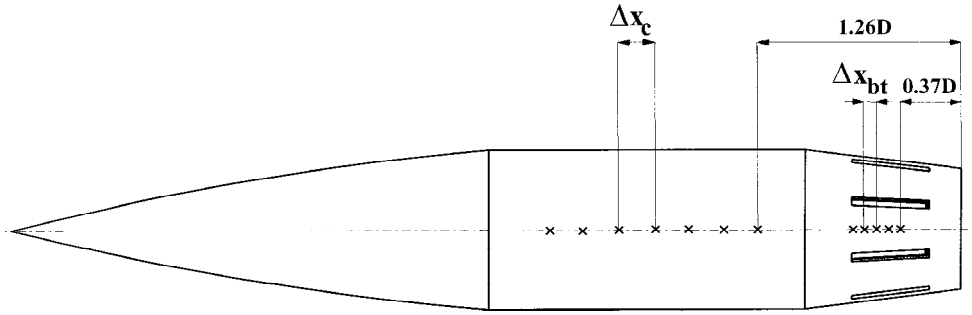

Fig. 2 Positions of the pressure taps on *M*1, Δx_c=(0.21÷0.245)*D* and Δx_{bt}=(0.07÷0.086)*D*

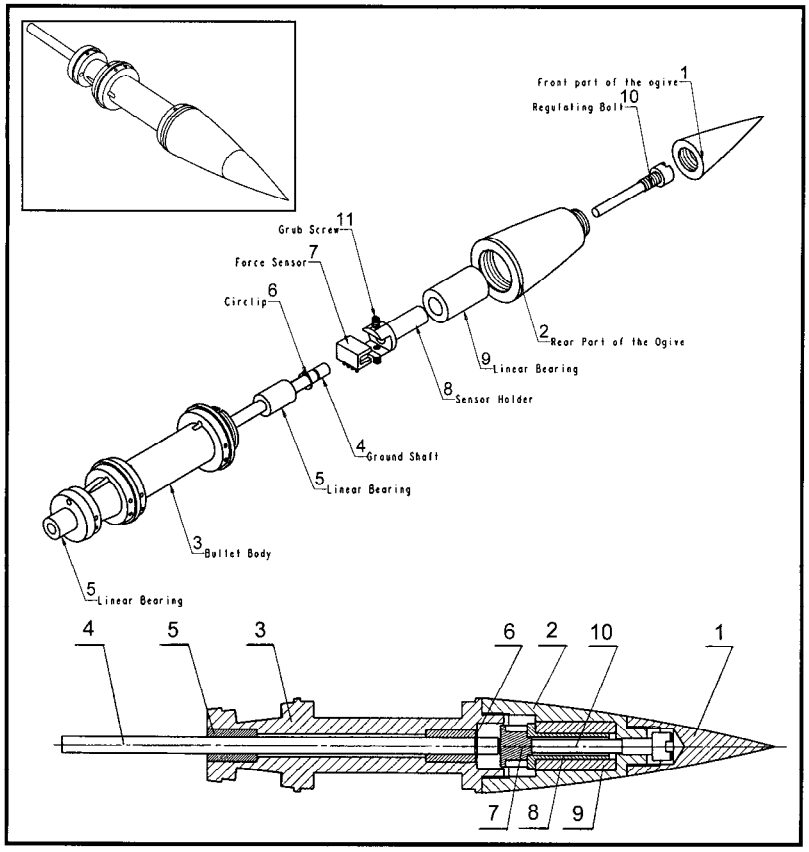

Fig. 3 Assembly drawing of model M2

a) M1 inside the wind tunnel test section

b) The used Models

Fig. 4 Photos of the test section and the models

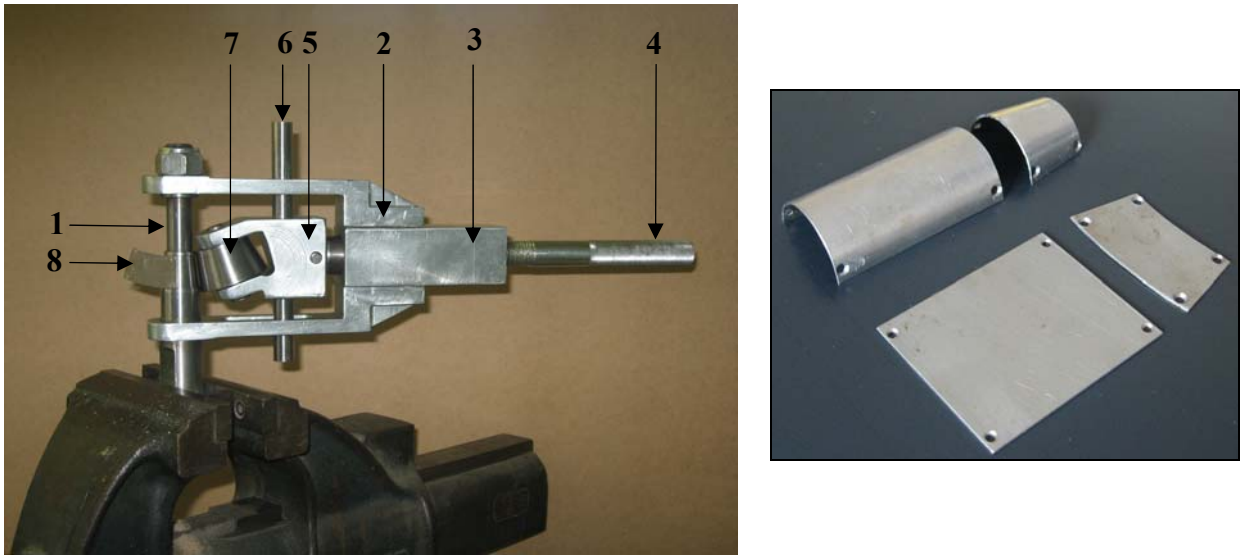

a) Rolling tool **b) Skins before and after rolling**

Fig. 5 Rolling the skins

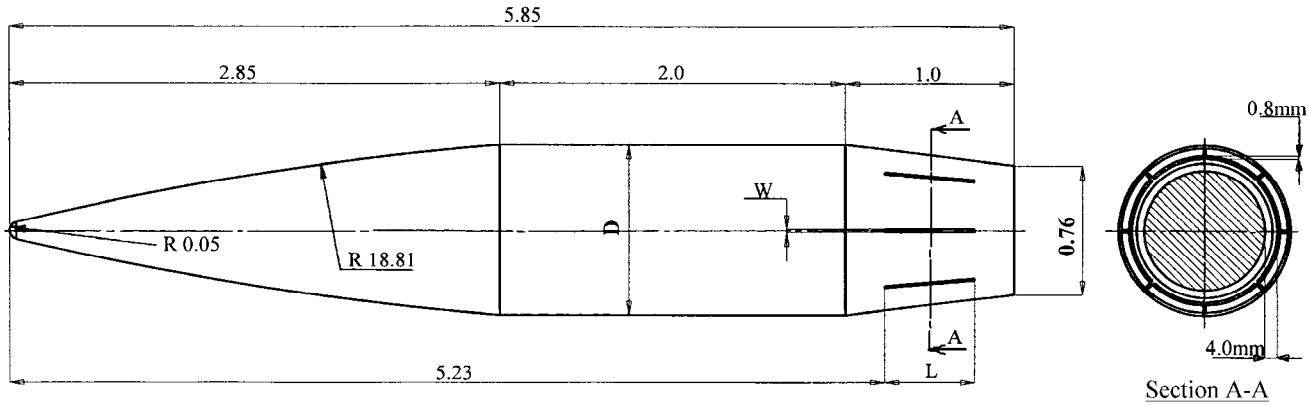

Fig. 6 Relative dimensions of SOCBT projectile

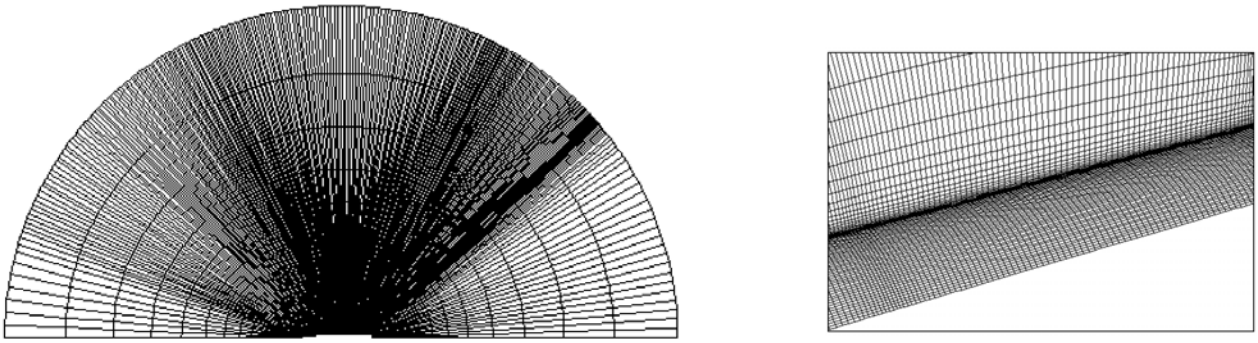

Figure 7 Three-dimensional grid for the solid-wall projectile**.**

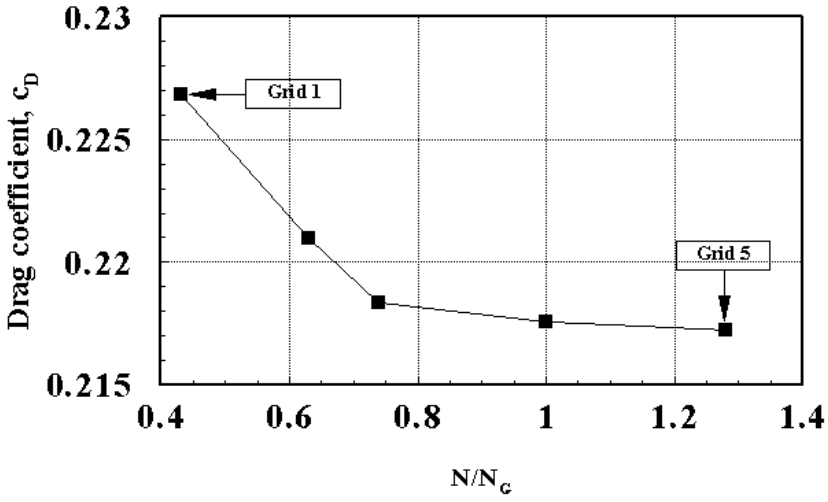

Figure 8 Variation of total drag coefficient for the tested grids at M = 0.96.

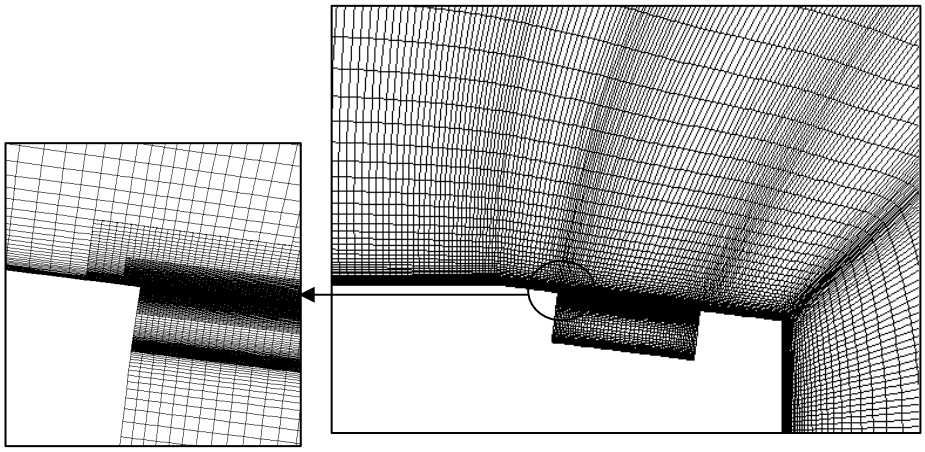

Fig. 9 Mesh refinement around the slot

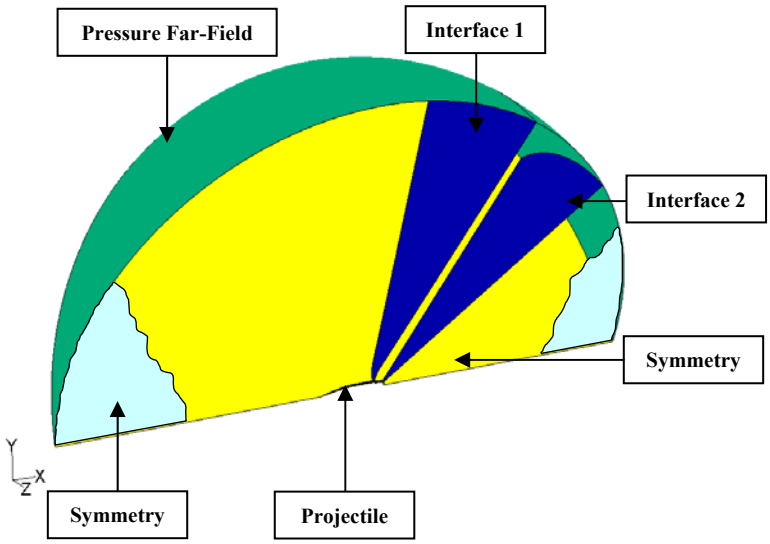

Fig. 10 Mesh boundary conditions

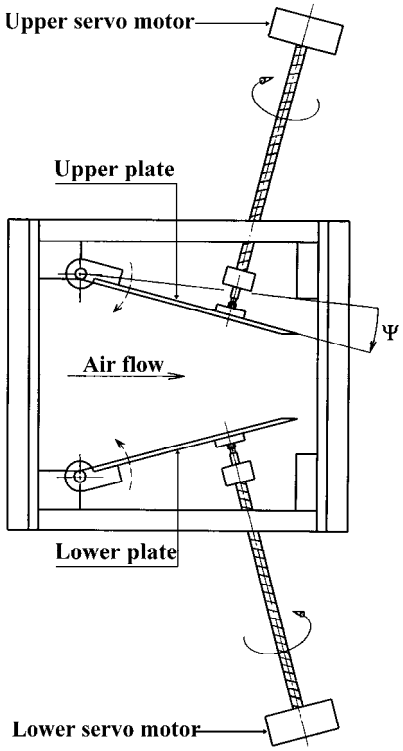

Fig. 11 Mechanism of the second nozzle setting

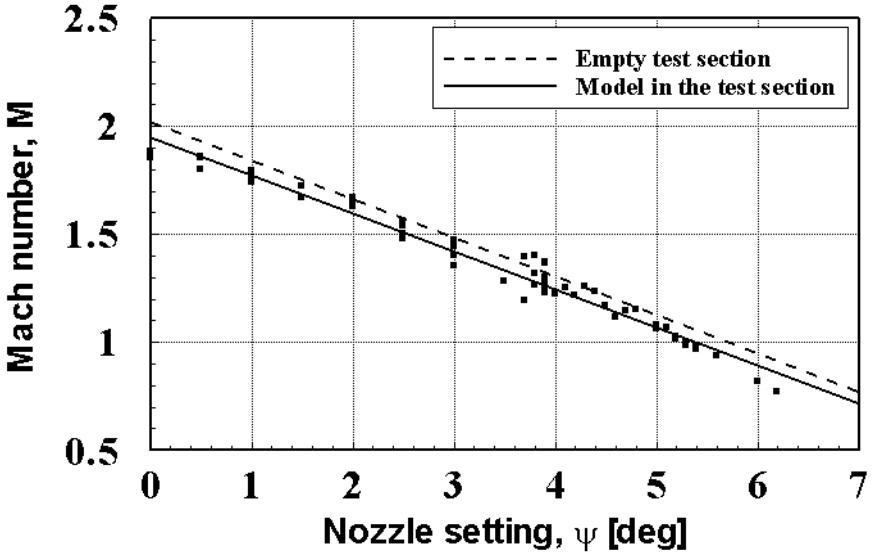

Fig. 12 Calibration of the wind tunnel with the supersonic liners

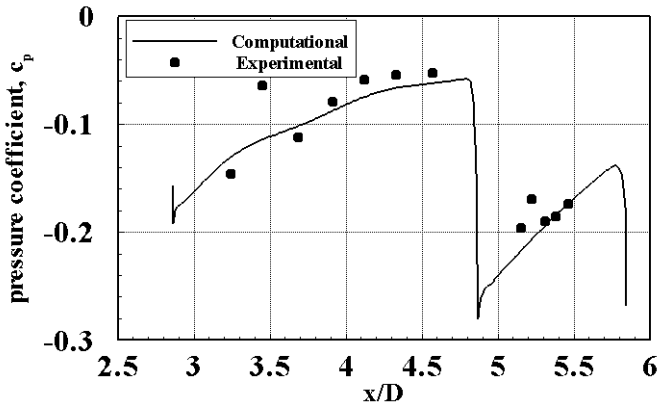

a) Solid (cylindrical and boat-tail sections)

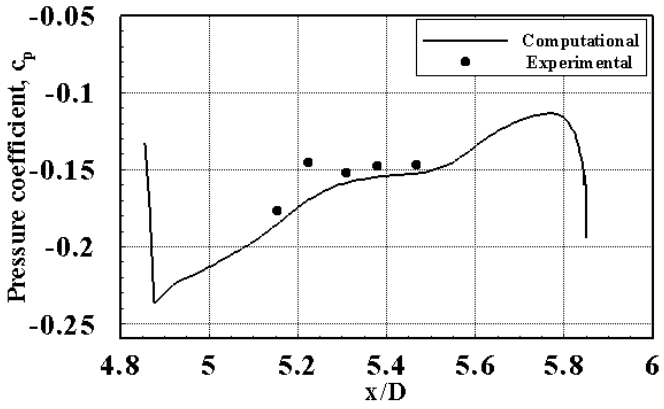

b) Slotted boat-tail, *W*=0.5 mm

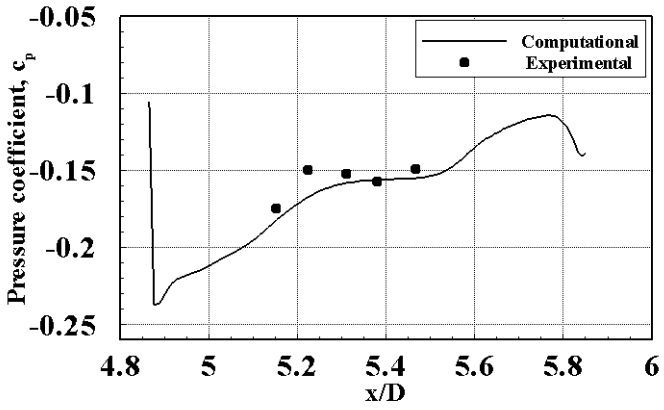

c) Slotted boat-tail, *W*=2.0 mm

Fig. 13 Comparison between measured and calculated pressure coefficients past the cylindrical and boat-tail sections at *M*=1.36.

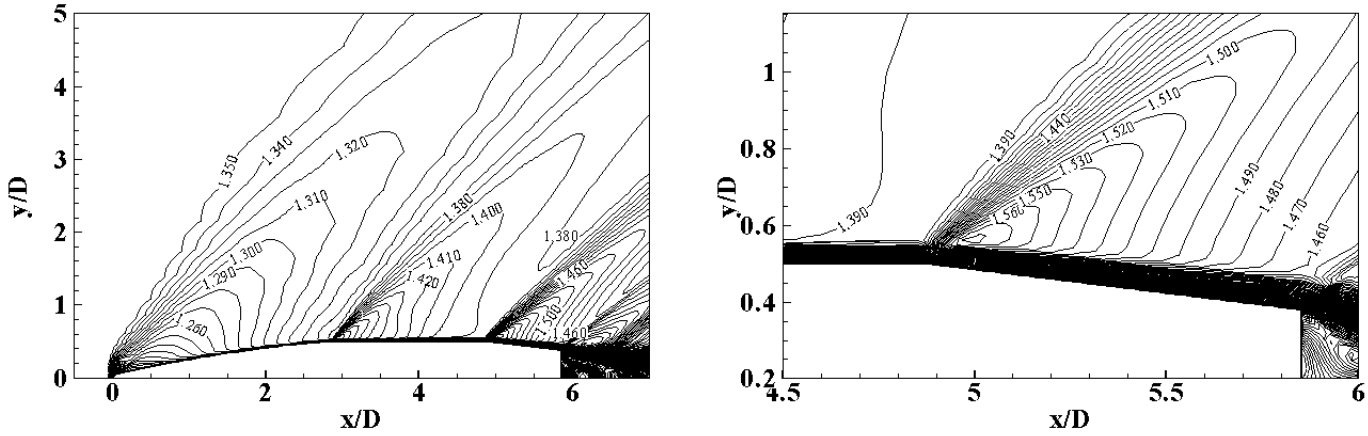

a) Solid-wall

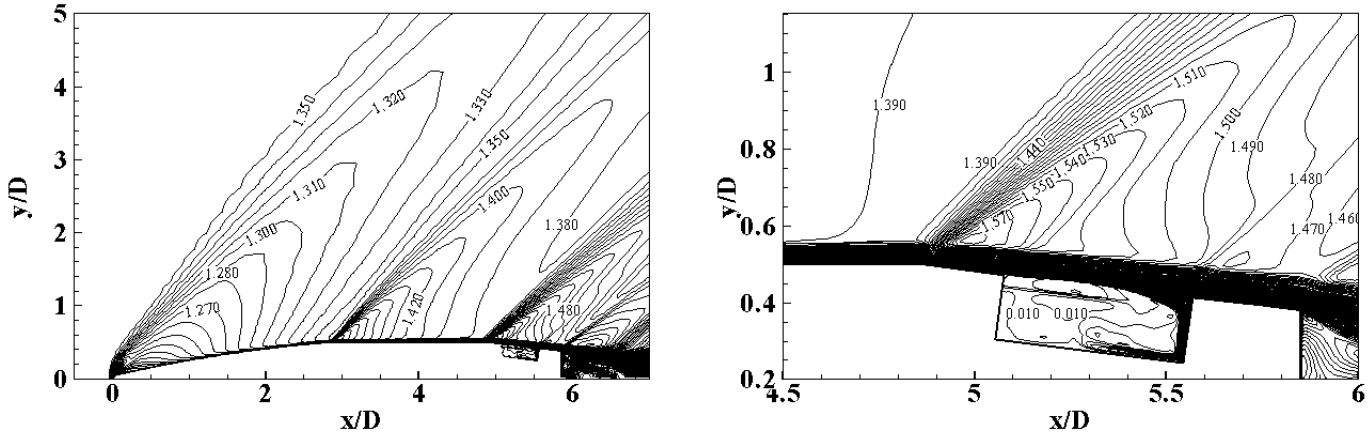

b) Slotted boat-tail, *W*=0.5 mm

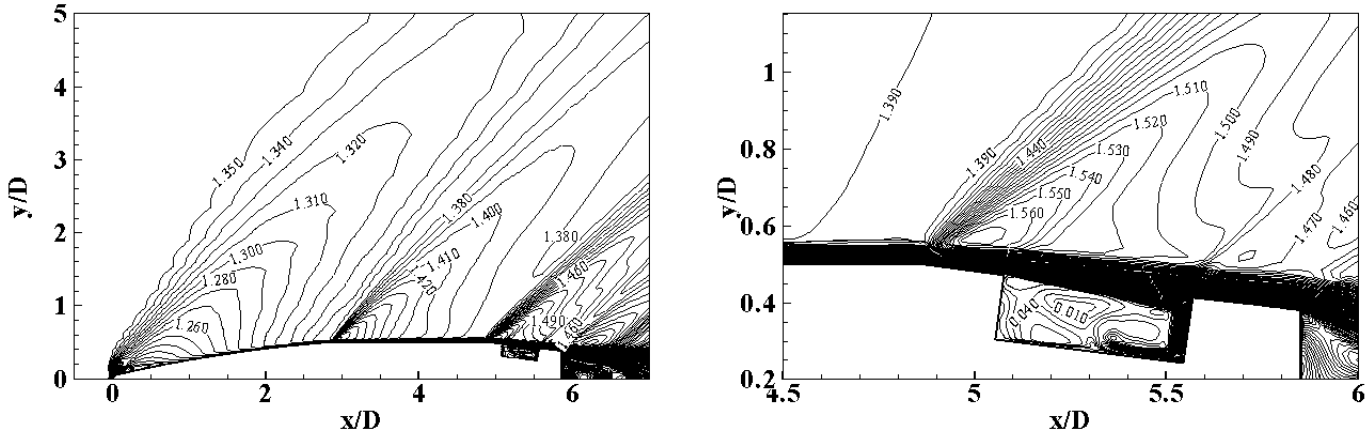

c) Slotted boat-tail, *W*=2.0 mm

Fig. 14 Mach contours over the solid and slotted boat-tails at *M*=1.36

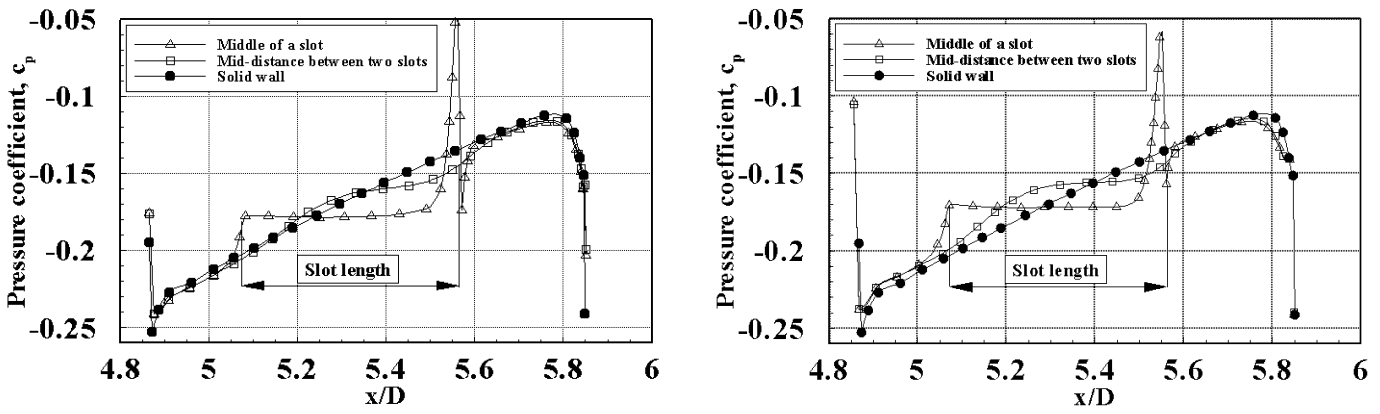

a) *W*=0.5 mm **b) *W*=2.0 mm**

Fig. 15 Pressure coefficient past solid and slotted-wall boat-tails at *M* = 1.36

a) *W*=0.5 mm

b) *W*=2.0 mm

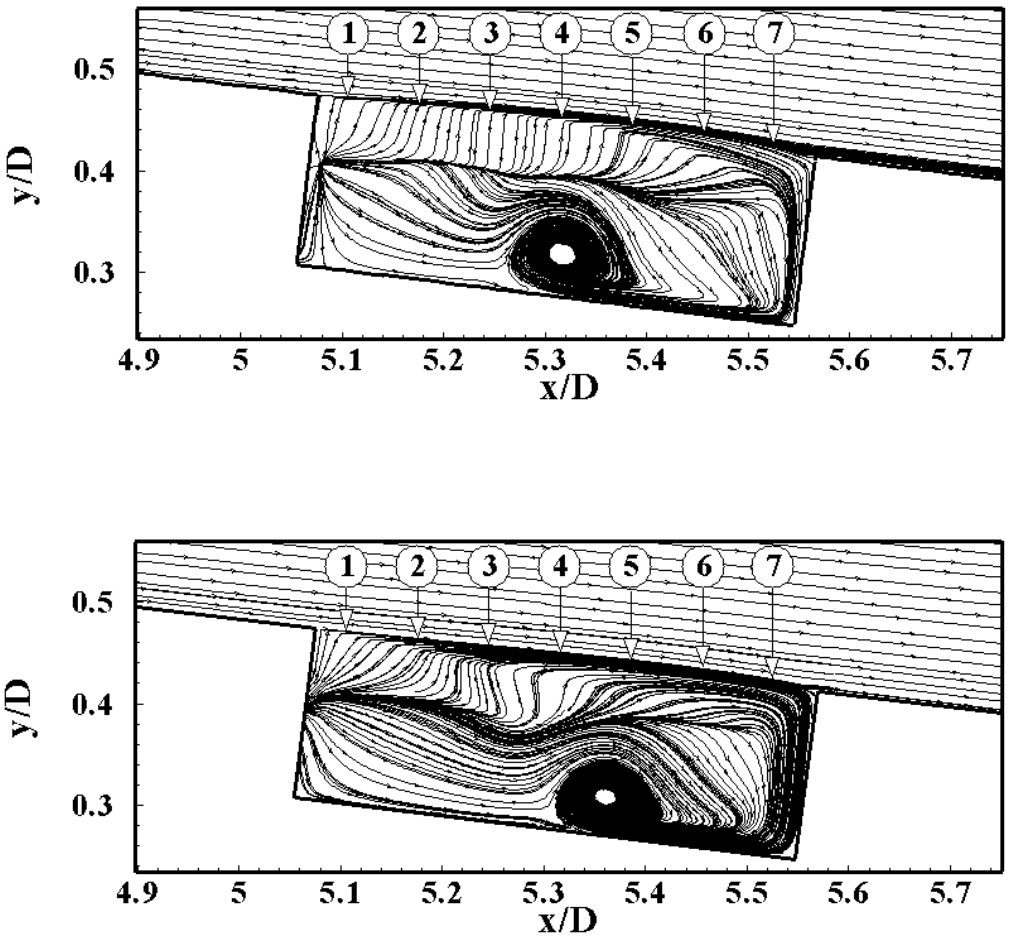

Fig. 16 Stream lines along a vertical plane passing through the middle of the slot at *M*=1.36

S.1

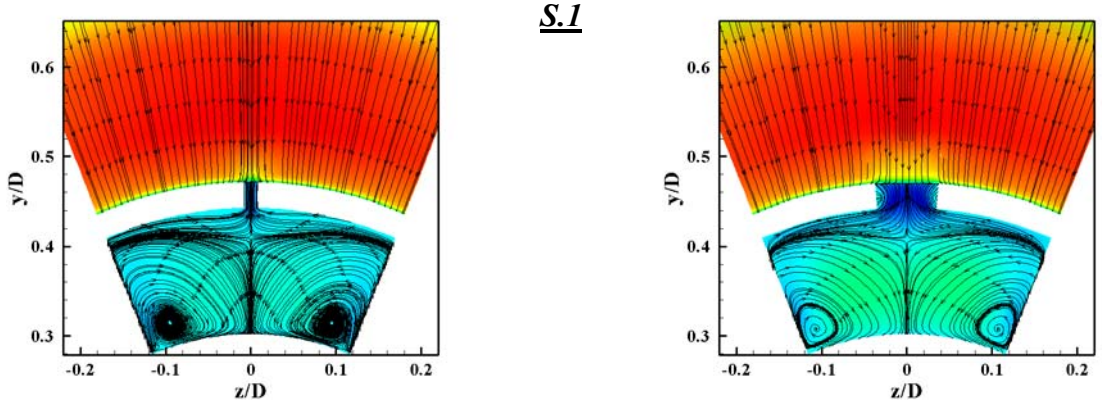

S.2

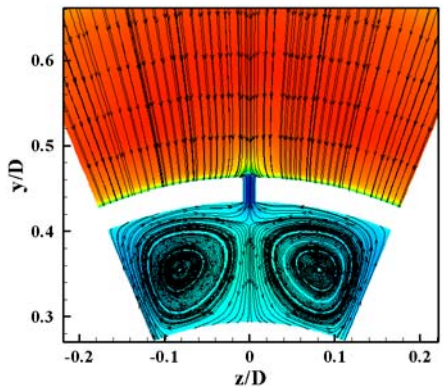
y/D
z/D
0.6
0.5
0.4
0.3
-0.2
-0.1
0
0.1
0.2

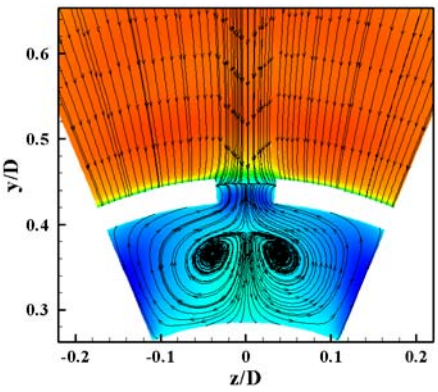
y/D
z/D
0.6
0.5
0.4
0.3
-0.2
-0.1
0
0.1
0.2

S.3

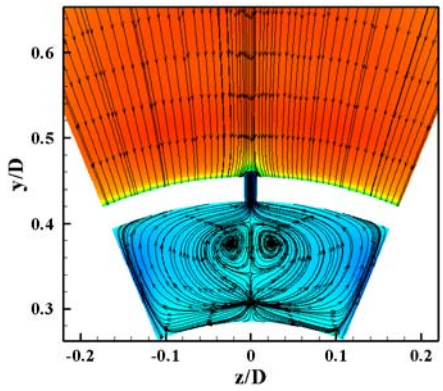
y/D
z/D
0.6
0.5
0.4
0.3
-0.2
-0.1
0
0.1
0.2

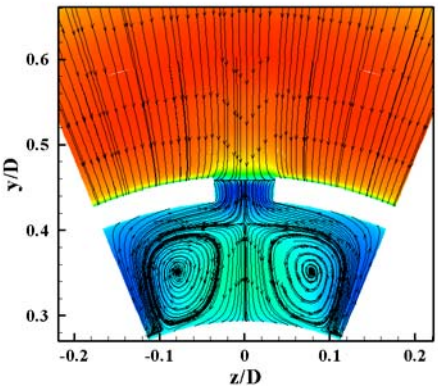
y/D
z/D
0.6
0.5
0.4
0.3
-0.2
-0.1
0
0.1
0.2

S.4

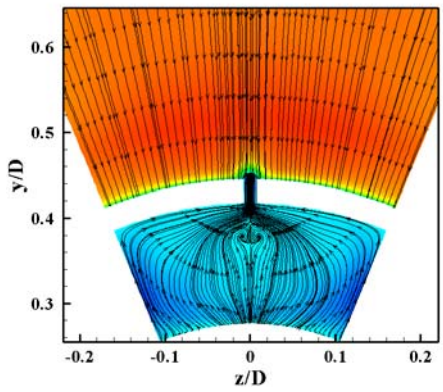
y/D
z/D
0.6
0.5
0.4
0.3
-0.2
-0.1
0
0.1
0.2

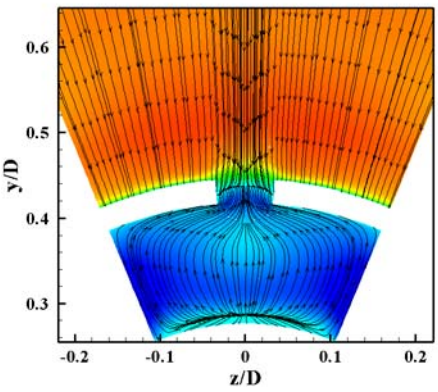
y/D
z/D
0.6
0.5
0.4
0.3
-0.2
-0.1
0
0.1
0.2

S.5

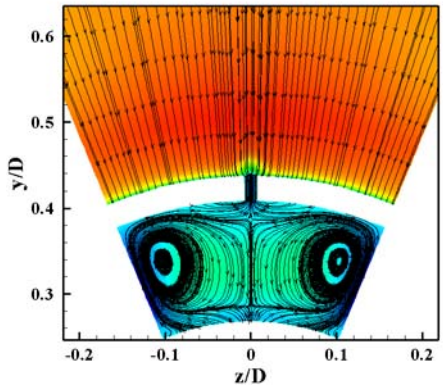
y/D
z/D
0.6
0.5
0.4
0.3
-0.2
-0.1
0
0.1
0.2

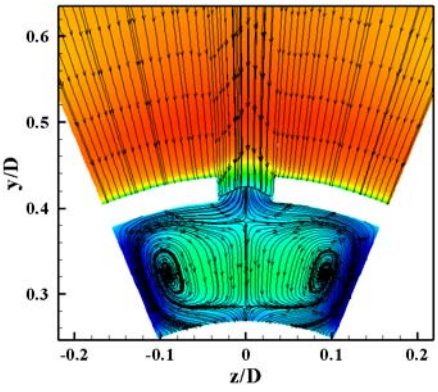
y/D
z/D
0.6
0.5
0.4
0.3
-0.2
-0.1
0
0.1
0.2

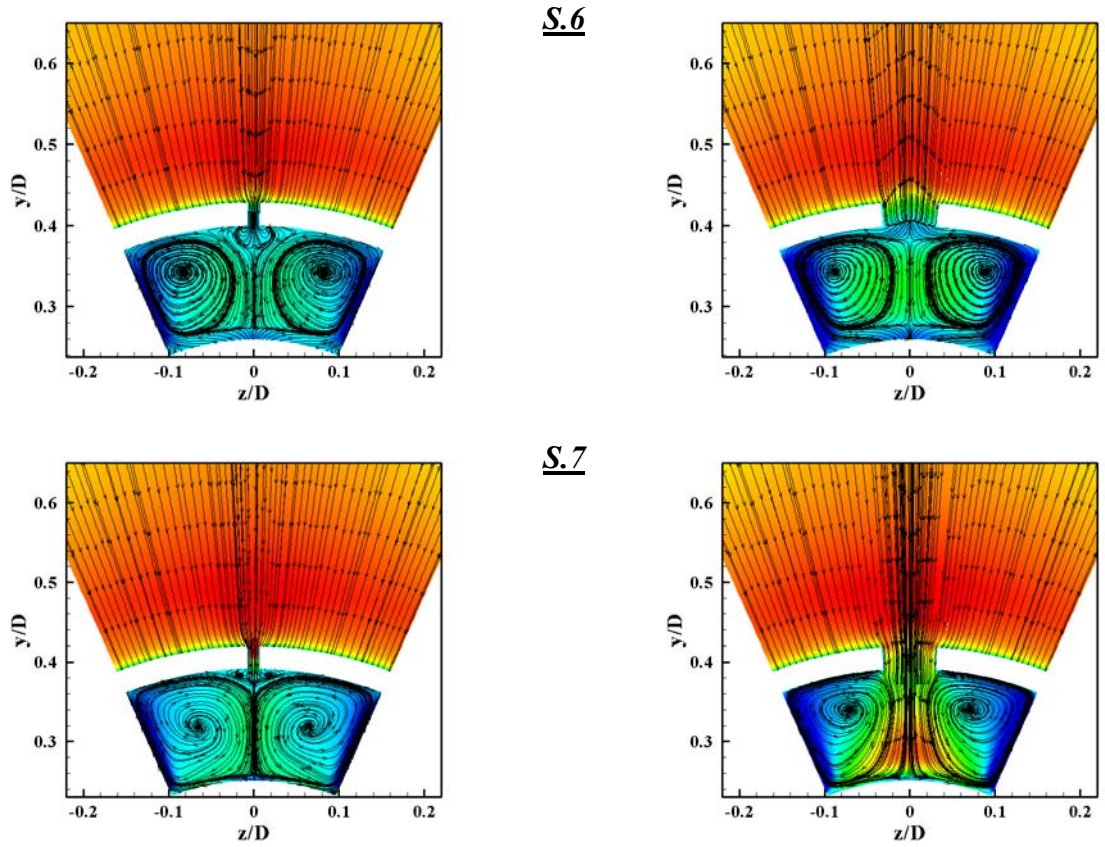

a) *W*=0.5 mm **b) *W*=2.0 mm**

Fig. 17 v-w stream lines at different stations passing through the cavity at M=1.36

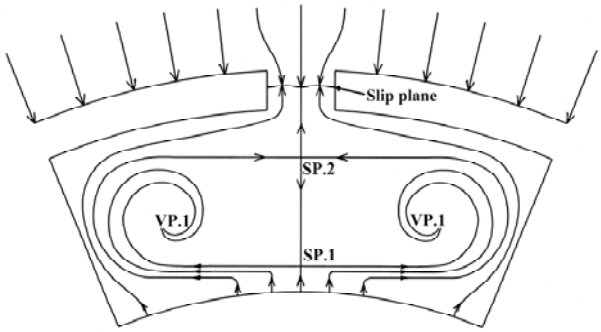

Fig. 18 Typical sketch of streamlines at S.1 to S.6 at *W*=0.5mm and S.1 to S.5 at *W*=2.0mm

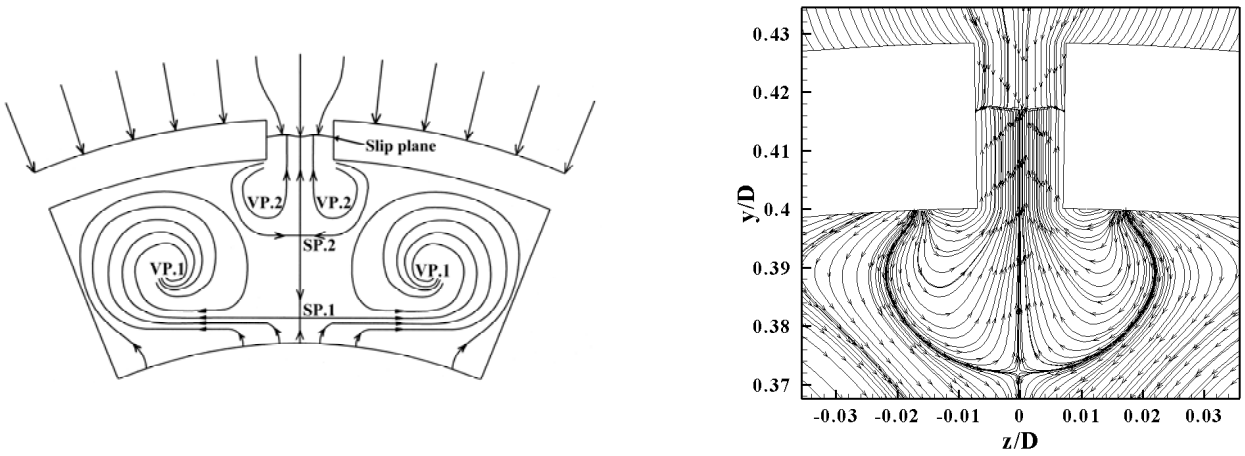

a) Sketch of streamlines **b) Zooming at VP.2**

Fig. 19 Flow pattern at S.6 in case of *W*=0.5 mm

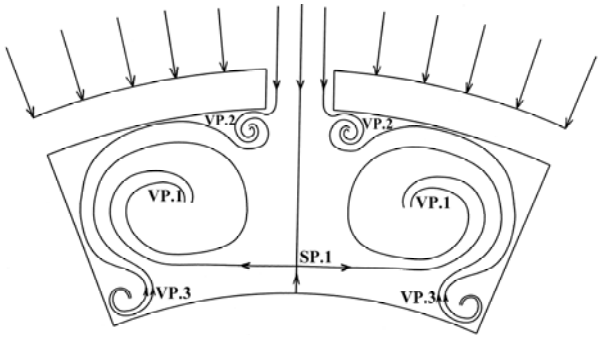

Fig. 20 Sketch of streamlines at S.7 in case of *W*=0.5 mm

a) Zooming at VP.2 **b) Zooming at VP.3**

Fig. 21 Zooming of streamlines at S.7 showing secondary and tertiary vortices

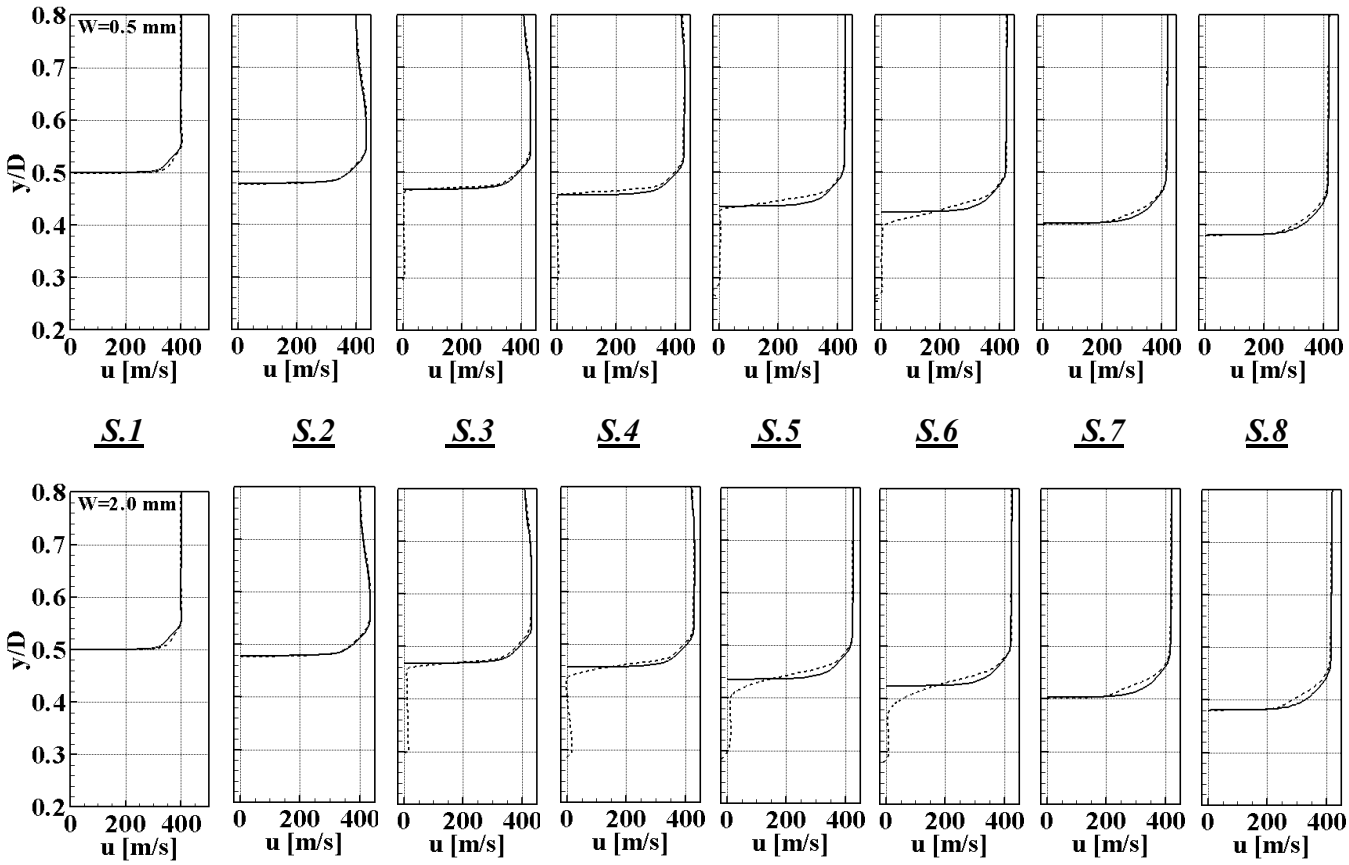

Fig. 22 Boundary layer velocity profiles past both solid and slotted boat-tails at *M*=1.36

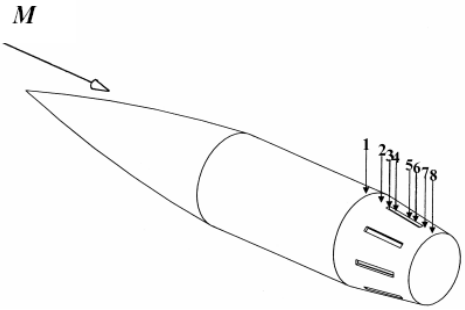

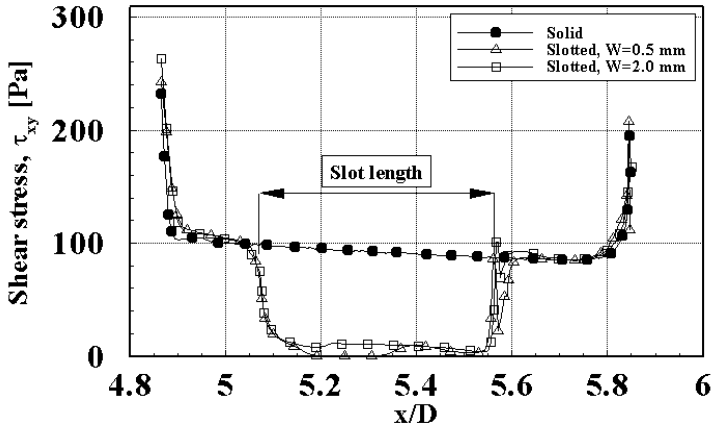

Fig. 23 Viscous shear stress on solid and slotted boat-tails along the slot centre

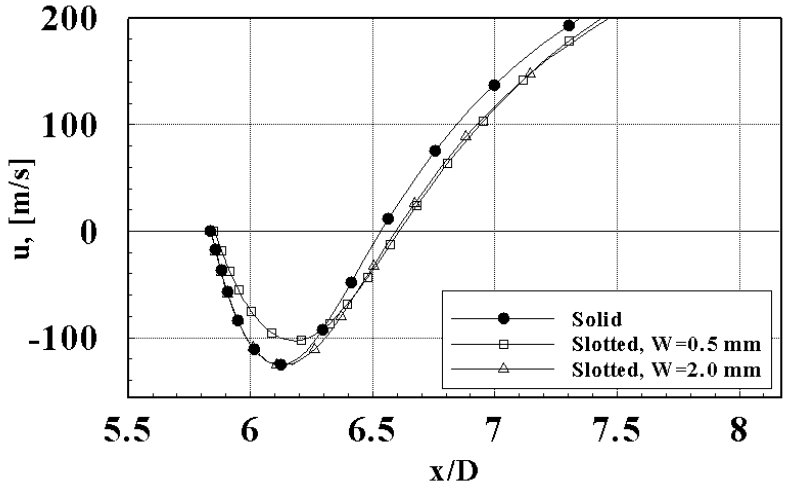

Fig. 24 Axial velocity behind the base

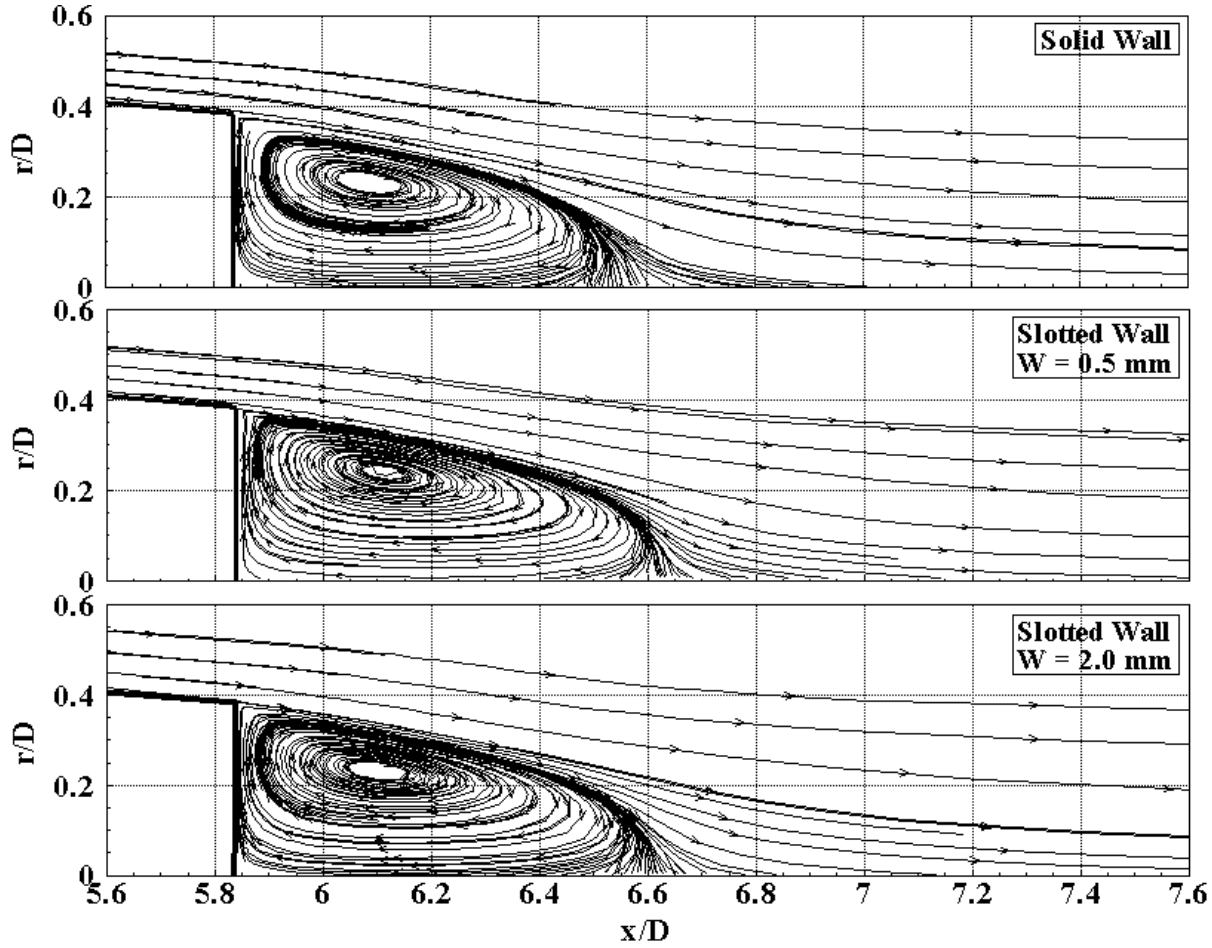

Fig. 25 u-v streamlines behind the base in the near wake region

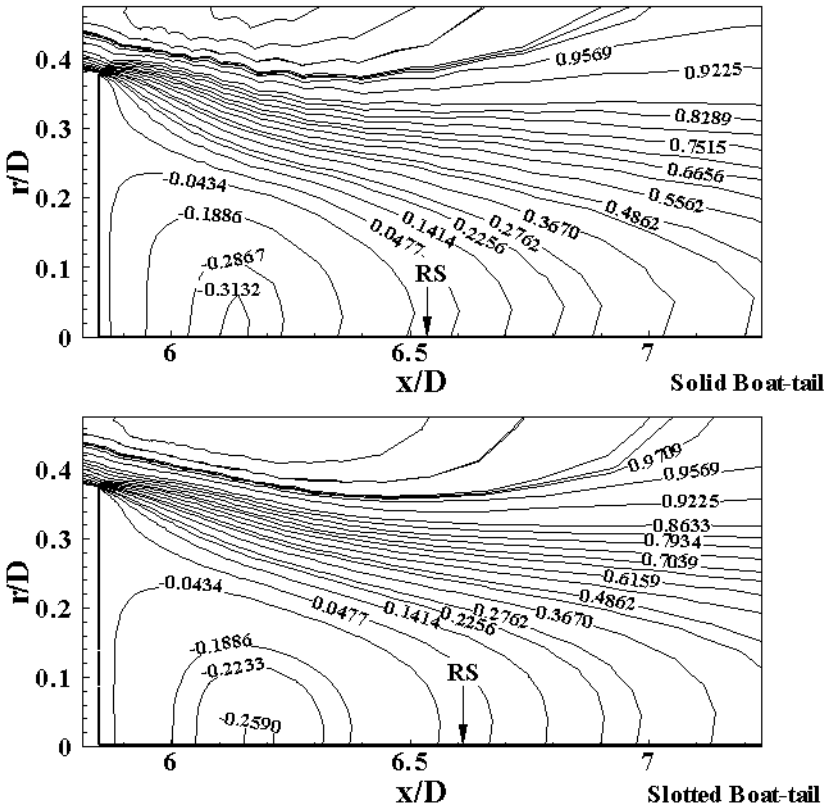

Fig. 26 Contours of axial velocity component (u/U_∞) behind the base

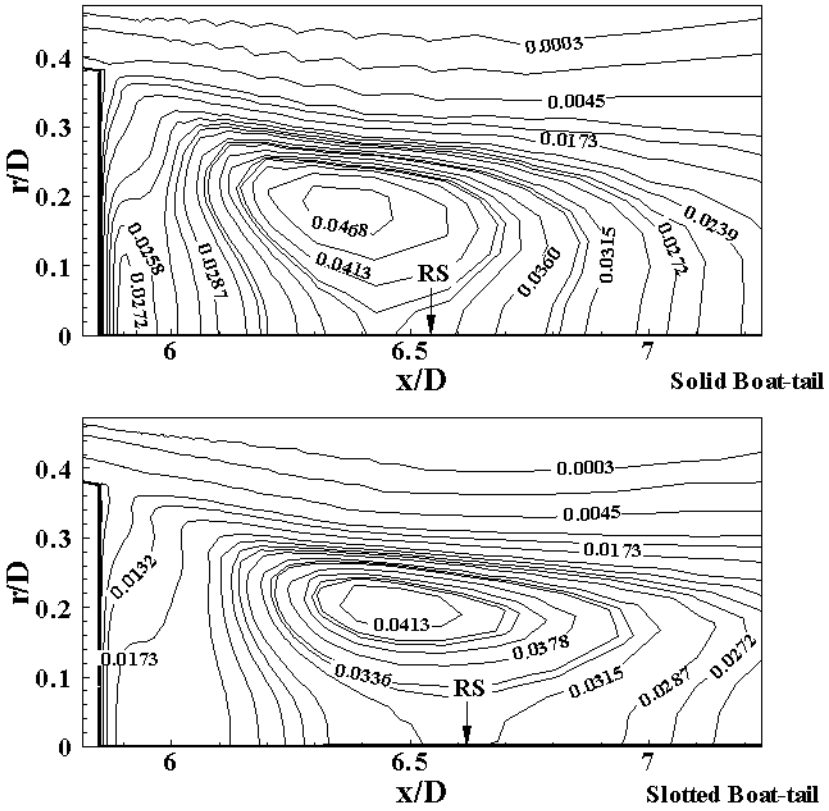

Fig. 27 Contours of turbulent kinetic energy $\left(k/U_\infty^2\right)$ behind the base

Table 1 Properties of the boundary layer velocity profile at the base corner

Bullet type	δ [mm]	δ^* [mm]	θ [mm]	H
Base line model	5.575	0.905	0.392	2.309
Slotted-boat-tail, *W*=0.5 mm	3.688	0.610	0.232	2.629
Slotted-boat-tail, *W*=2.0 mm	3.330	0.653	0.244	2.676

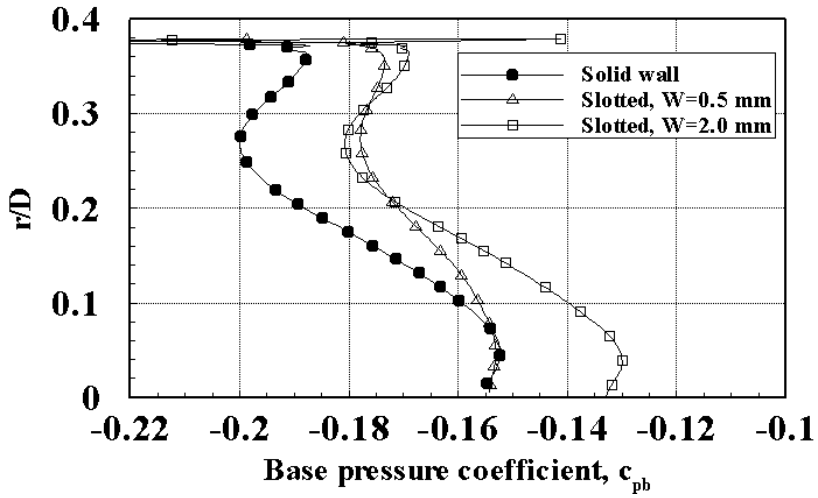

Fig. 28 Pressure coefficient behind the base for both solid and slotted boat-tails

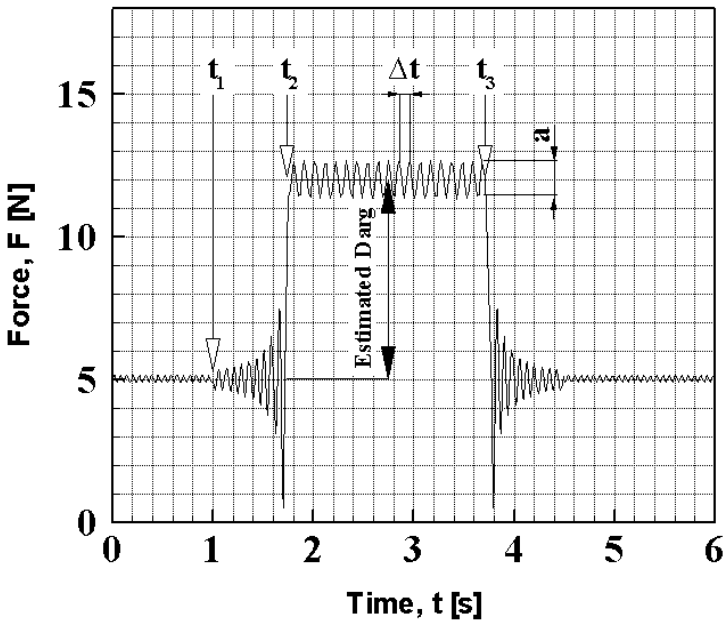

Fig. 29 Typical response of force measurement

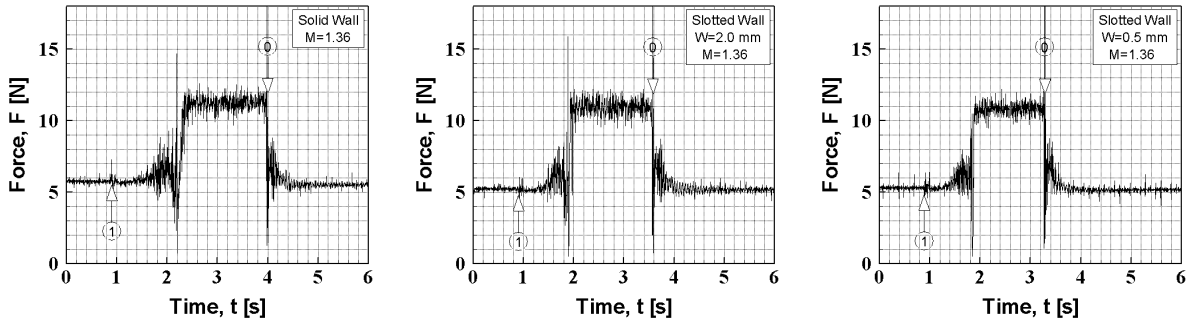

a) Force measurement at M =1.36

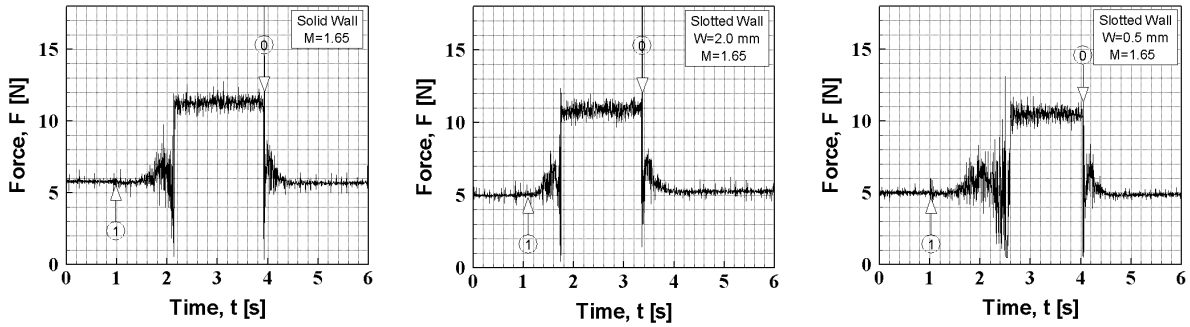

b) Force measurement at M =1.65

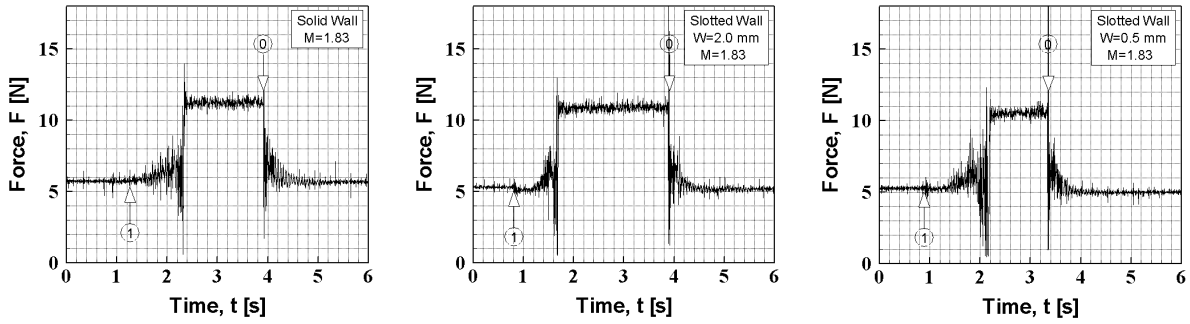

c) Force measurement at M =1.83

Fig. 30 Force measurement for both of the solid and slotted projectiles

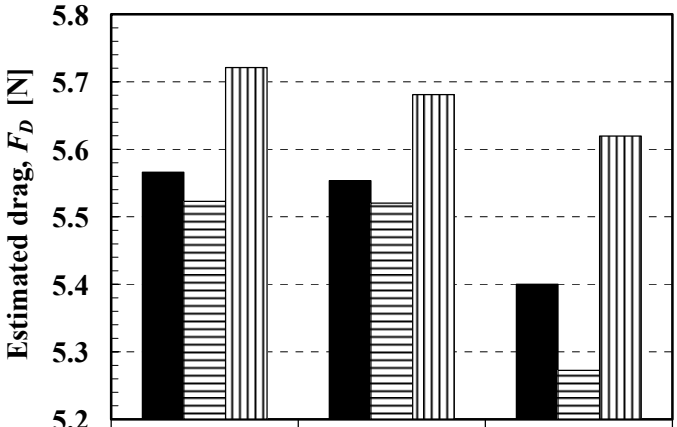

	M=1.36	M=1.65	M=1.83
■ Solid	5.56614	5.55360	5.40000
▤ Slotted, W=0.5 mm	5.52276	5.52030	5.27256
▥ Slotted, W=2.0 mm	5.72100	5.68098	5.61960

Fig.31 Comparison between the measured drag in case of solid and slotted-wall bullets

Table 2 Drag components on both solid and slotted-wall boat-tails at M=1.36

Bullet type	Drag coefs.	Bullet parts				c_d	D [N]
		Ogive	Cylinder	Boat-tail	Base		
Base line model	c_{dp}	0.09231	≈0	0.07154	0.11035	0.32705	8.64
	c_{dsf}	0.02333	0.02156	0.00796	≈0		
	$\sum$	0.11564	0.02156	0.07950	0.11035		
Slotted-boat-tail, W=0.5 mm	c_{dp}	0.09261	≈0	0.07187	0.10040	0.32033	8.53
	c_{dsf}	0.02419	0.02286	0.00840	≈0		
	$\sum$	0.11680	0.02286	0.08027	0.10040		
Slotted-boat-tail, W=2.0 mm	c_{dp}	0.09255	≈0	0.07362	0.09816	0.31724	8.48
	c_{dsf}	0.02373	0.02158	0.00760	≈0		
	$\sum$	0.11628	0.02158	0.081224	0.09816		